Journal of Glaciology



Article

Cite this article: Voermans JJ, Rabault J, Marchenko A, Nose T, Waseda T, Babanin AV (2023). Estimating the elastic modulus of landfast ice from wave observations. *Journal of Glaciology* 1–11. https://doi.org/10.1017/ jog.2023.63

Received: 10 May 2023 Revised: 4 July 2023 Accepted: 20 July 2023

Keywords:

Glaciological instruments and methods; ice/ocean interactions; sea ice

Corresponding author:

Joey J. Voermans; Email: jvoermans@unimelb.edu.au

© The Author(s), 2023. Published by Cambridge University Press on behalf of The International Glaciological Society. This is an Open Access article, distributed under the terms of the Creative Commons Attribution licence (http://creativecommons.org/licenses/ by/4.0/), which permits unrestricted re-use, distribution and reproduction, provided the original article is properly cited.

cambridge.org/jog

Estimating the elastic modulus of landfast ice from wave observations

Joey J. Voermans¹, Jean Rabault², Aleksey Marchenko³, Takehiko Nose⁴, Takuji Waseda⁴ and Alexander V. Babanin¹

¹Department of Infrastructure Engineering, University of Melbourne, Melbourne, Australia; ²Norwegian Meteorological Institute, Oslo, Norway; ³Arctic Technology Department, The University Centre in Svalbard, Longyearbyen, Norway and ⁴Graduate School of Frontier Sciences, The University of Tokyo, Kashiwa, Chiba, Japan

Abstract

Progress in our understanding of wave-ice interactions is currently hindered by the lack of in situ observations and information of sea-ice properties, including the elastic modulus. Here, we estimate the effective elastic modulus of sea ice using observations of waves in ice through the deployment of three open-source geophone recorders on landfast sea ice. From observations of low-frequency dispersive waves, we obtain an estimate of the effective elastic modulus in the range of 0.4–0.7 GPa. This is lower than the purely elastic modulus of the ice estimated at 1 GPa as derived from in situ beam experiments. Importantly, our experimental observation is significantly lower than the default value currently in use in wave models. While our estimate is not representative for all sea ice, it does indicate that considerably more measurements are required to provide confidence in the development of parameterizations for this complex sea-ice property for wave models.

Introduction

Waves can propagate hundreds of kilometers into the sea ice before the majority of their energy is attenuated by wave scattering (Kohout and Meylan, 2008; Montiel and others, 2016) and wave dissipation processes, including turbulence (Kohout and others, 2011; Voermans and others, 2019; Herman, 2021), internal friction (Wang and Shen, 2010), overwash (Nelli and others, 2020) and ice-floe collisions (Herman and others, 2019; Rabault and others, 2019; Løken and others, 2022). The rate of attenuation is largely determined by the properties of the ice cover. When the wave steepness is sufficiently high, waves can break the ice (Dumont and others, 2011; Voermans and others, 2020), thereby reducing its attenuation capacity and allowing waves to penetrate farther into the ice cover, ultimately progressing the distance of break-up activity into the ice (e.g. Collins and others, 2015). Implementation of these complex feedbacks between the waves and the ice in our forecasting models is strongly dependent on our collective knowledge of the physical processes describing wave-ice interactions (e.g. Boutin and others, 2020; Kousal and others, 2022; Nose and others, 2023).

Many theories and models currently exist to describe wave-ice interactions, with varying degree of complexity and representation of the underlying wave-ice physical processes (e.g. see Shen, 2019; Squire, 2020; Rogers and others, 2021, for an overview). All these models rely in one way or another on the properties of the ice. Notable sea properties are the ice thickness and elastic modulus, but others include the flexural strength, roughness (both above and below the waterline) and horizontal dimensions of the ice floes. Validation of the theories and models against field experimental observations is however very limited, largely due to the difficulty of obtaining synchronous observations of waves and sea ice in the field.

Measuring waves and sea-ice properties is hindered by the extreme complexity of this harsh environment which poses logistical and technological challenges. Despite this, significant progress has been made in measuring waves in sea ice due to developments and advancements in low-cost instrumentation (e.g. Rabault and others, 2022) and satellite-derived products (Ardhuin and others, 2015; Horvat and others, 2020), which already has led to a substantial increase of the availability of in situ wave observations (Rabault and others, 2023). In contrast, access to observations of the physical and mechanical properties of sea ice remains restricted, with the exception perhaps of sea-ice thickness which may be estimated from satellite-derived products (e.g. Pațilea and others, 2019). Importantly, the elastic modulus remains a sparingly documented property of sea ice in relation to wave-ice interaction studies.

The elastic modulus *E* is equal to the ratio of the stress and strain in the ice sheet during elastic behavior (Timco and Weeks, 2010). When considering most engineering applications, however, the ice does not behave as purely elastic and delayed elasticity may become important during small loading rates. We may define the total recoverable strain as the sum of the purely elastic strain and the delayed strain, denoted by an effective elastic modulus E^* (Williams and others, 2013). Timco and Weeks (2010) suggest typical values of the effective elastic modulus between 1 and 5 GPa, where Williams and others (2013) opt for a somewhat higher value of 4–7 GPa, and Karulina and others (2019) a lower value with observations between 0.3 and 4 GPa. Due to the limited observational data of E^* , the default value in contemporary wave models is

Check fo

currently 5.5 GPa (WW3DG, 2019) which, by lack of better alternatives, is commonly adopted in wave-related studies in the Marginal Ice Zone (MIZ) (e.g. Williams and others, 2017; Boutin and others, 2018; Li and others, 2021). This poses several problems. First, the elastic modulus may vary drastically across spatial and temporal scales due to differences in growth history and local environmental conditions. For example, drifting sea ice in the Antarctic MIZ is unlikely to exhibit the same sea-ice properties as thin landfast ice in an Arctic fjord does. Second, it provides an additional tuning parameter to fit model output to the observations, thereby potentially masking the mechanistic output of the models or, in other words, it obscures our qualitative understanding of wave-ice interactions (e.g. Voermans and others, 2021). Lastly, an unknown elastic modulus leads to quantitative uncertainty in the model output including critical system dynamical variables, such as the MIZ width. For example, choosing wave scattering as an attenuation model, Williams and others (2017) showed in their numerical experiments that a doubling of the effective elastic modulus may double the MIZ width during swell events. We note that an uncertainty of E^* by a factor of two (or even more) is far from uncommon as in most wave-ice studies E^* is not measured nor inferred. The sensitivity of the wave-ice interaction models to the properties of the ice, and thus their collective outcome and feedback into the dynamics of a wave-ice coupled system, highlights the desperate need for more frequent and accurate observations of sea-ice properties.

Traditional methods of measuring the elastic modulus of sea ice tend to be laborious, whether by testing sea-ice samples, or in situ through ice beam experiments (Timco and Weeks, 2010; Karulina and others, 2019; Marchenko and others, 2020). Ideally, sea-ice properties are inferred from long-term in situ sensor deployments without the requirement of continuous human presence, which would then allow for higher temporal and/or spatial resolution of such observations. The elastic modulus of sea ice can be estimated based on observations of the propagation speed of waves in the ice (Yang and Giellis, 1994; Stein and others, 1998; Moreau and others, 2020a). This can be inferred from the phase speeds of flexural waves, compressive and/or shear waves and typically involves the deployment of accelerometers, seismometers or geophones to track the waves in the spatial domain (e.g. Oliver and others, 1954; Yang and Giellis, 1994; Sutherland and Rabault, 2016; Moreau and others, 2020a). Recent studies have shown that several sea-ice properties, such as, the ice thickness, Poisson's ratio and elastic modulus, can be estimated from sea-ice vibration observations obtained from geophones in great detail (Moreau and others, 2020a, 2020b; Serripierri and others, 2022; Moreau and others, 2023). Progresses in instrument autonomy, and the identification and processing of vibration data makes geophones instrumental to increase the dataset of in situ observations of the elastic modulus across the polar regions. This then, we expect, will significantly improve our understanding of wave-ice interactions which are closely linked to this difficult to measure property.

In 2022 we deployed, among others, three geophones on landfast sea ice in Tempelfjorden, Svalbard, to study wave-ice interactions. Several locally generated low-frequency dispersive flexural waves were observed during the experiment, covering a relatively wide frequency range of 0.08–0.28 Hz. We use this opportunity to use low-frequency wave observations to estimate the effective elastic modulus of the landfast sea ice during this measurement campaign. We show that the effective elastic modulus estimated from our experimental observations is significantly lower than the default value typically employed in wave models. While we stress that our estimate is not representative for all sea ice, it indicates that considerably more measurements are required to provide confidence in the development of parameterizations of this complex and important property of sea ice for implementation in wave models.

Methods

Experimental setup

To measure waves in sea ice, various instruments were deployed on landfast sea ice from 11 to 28 February 2022 in Tempelfjorden, Svalbard. The experimental setup consist of multiple ice buoys (Rabault and others, 2020), one hydrophone (Audiomoth Dev v1.0.0. with an Aquarian Audio h2a hydrophone) and three geophone loggers. The ice buoys focus on the frequency range between 0.05 and 1 Hz (i.e. ocean waves), whereas the geophones target sea-ice vibrations with frequencies up to 240 Hz. The hydrophone logger was deployed to record the acoustic radiation of ice events underwater, such as cracking and break-up, with a sampling rate of 48 kHz. The ice motion loggers were deployed along a line parallel to the main axis of the fjord and the geophones were deployed closest to the glacier-side of the fjord in triangular formation with sides of ~200 m. The distance between the geophones needs to be large enough to record the fastest waves, such as compressive and/or shear waves which have phase speed of a few thousand meters per second, but small enough to limit significant wave transformation and wave attenuation effects over this distance. The hydrophone was deployed next to the geophone closest to the open water (see Fig. 1). In this study, no data from the ice buoys were used as the measured wave energy during the measurement campaign was very small.

Ice thickness was measured at the sites of the ice buoys at the time of deployment. The thickness was 35, 40, 47 and 52 cm in the direction from the open water toward the glacier, respectively (see Fig. 1). The thickness did not change noticeably over the duration of the experiment. Air temperatures measured at Svalbard Lufthavn (45 km from the deployment site) varied between -27 and -5° C. The local water depth is ~40 m at the site (Marchenko and others, 2013).

Geophone logger

A custom geophone logger was designed for this project to record sea-ice vibrations. While various low-cost and open-source designs are available to record the analog signals of the geophones, such as the Geophonino of Soler-Llorens and others (2016), we developed a custom logger instead for general

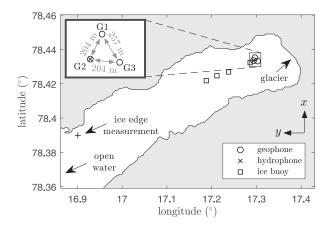


Figure 1. Experimental setup in Tempelfjorden, Svalbard. Instrument deployment consists of three geophone logger (also see inset), a hydrophone and four wave-ice buoys. In situ cantilever experiments were performed near the ice edge, marked by the '+' sign.

flexibility and to suit our experimental design. Most notably, the logger was designed to record five analog channels continuously at a sampling rate of 1000 Hz to an SD-card, including timestamps at high temporal accuracy (the order of microseconds) by using GPS time synchronization. The latter allows cross correlation between instruments without the need of instruments to communicate with each other or be connected to a centralized system.

The hardware of the instrument consists of five main components: (1) a microcontroller, Arduino Due; (2) SD-card breakout, used to store the recorded signals; (3) GPS breakout, used for time synchronization and recording of its location; (4) signal amplifiers, to amplify the voltage signals generated by (5) the geophone. Both firmware and design of the hardware are made open-source and can be found at http://github.com/jvoermans/Geophone_ Logger. A major advantage of this design is that it can be adapted and extended to facilitate on-board processing and satellite transmission capabilities.

Here, we used a triaxis GS-One 10 Hz geophone, which has a spurious frequency >240 Hz and sensitivity of 85.5 V s m⁻¹. Based on the datasheet, the geophone response is linear for f > 10 Hz, and decays exponentially for smaller frequencies. The geophones used in this study were not calibrated, meaning that the recorded voltages cannot be converted to surface elevation with sufficient accuracy. However, phase information of the recorded vibrations are unaffected. The *x*- and *y*-components of the geophones were amplified by a gain of 50, whereas the signal of the *z*-component was split and amplified by gains of 5, 50 and 1000 to increase the range of sensitivity of the logger. We note that the *z*-component of geophone 1 did not work for unknown reasons.

Elastic modulus

To provide comparison of our estimates of the effective elastic modulus, in situ beam experiments were performed on the ice to obtain independent estimates of the elastic modulus. It is known that eigenfrequency of flexural oscillations of a beam depends on the elastic modulus of the beam material and does not depend on the Poisson's ratio (Landau and Lifshitz, 1975). This fact leads to the method of calculation of the elastic modulus by the measuring the eigenfrequency of the beam oscillations. The first eigenmode maximum amplitude is reached in the center of the beam. Tests with floating vibrating beam with fixed-ends was introduced to measure the elastic modulus of floating ice in natural environment (Marchenko and others, 2020). The fixed-beam is formed by two through parallel cuts in floating ice (Fig. 2). In the test the motion of the beam is initiated by a hit in the beam center. Accelerations are measured by the accelerometer mounted at the beam surface. In the tests we used uniaxial accelerometers Bruel & Kjær DeltaTron Type 8344 designed to measure vibrations in the frequency range 0.2 Hz-3 kHz.

In contrast to free-free beam or fixed-fixed beam the eigenfrequency of the floating fixed-ends beam is not described by a simple analytical formula. Moreover, the eigenfrequency is complex because elastic energy of the oscillations radiates into the infinity. In addition, the added mass effect should be considered for the modeling of dynamic motions of the floating beam. In the present investigation the elastic modulus was adjusted to the measured frequency by modeling with finite-element software Comsol Multiphysics. Numerical simulations are described in the Supplementary material.

The floating fixed-ends beam was made near the edge of the landfast ice in the Temple Fjord (Fig. 2a) on 9th of March 2022 ~10 km from the geophones (Fig. 1). Preliminary, the ice surface was cleaned from a thin layer of snow. The ice thickness was H = 30 cm. The beam length was $L_b = 3$ m, and the beam width was b = 27 cm. The widths of through cuts in ice was of ~10 cm. We prepared round ends of the cuts using Kovacs drill with 10 cm diameter. The accelerometer was placed in the center of the beam and the beam motion was initiated by several hits by a stick near the beam center.

The ice temperature was measured using a temperature string (Geoprecision) with distance between neighbor thermistors of 5 cm (Fig. 3). The temperature string was placed in natural ice with thin snow layer at the surface. The surface temperature of ice was higher because snow was removed, and ice surface was slightly flooded. We think that ice temperature in the beam was varying between -2.5° C and freezing point of sea water -1.9° C. Sea ice in the Temple Fjord had columnar structure with diameter of a column of ~1 cm and larger (Fig. 4a). The horizontal thin section in Figure 4b indicated S2 type of ice. The ice salinity was 5 ppt. Speed of p-waves was measured of ~3 km s⁻¹.

Record of the beam accelerations is shown in Figure 5. Sampling frequency of the accelerometer was 20 kHz.

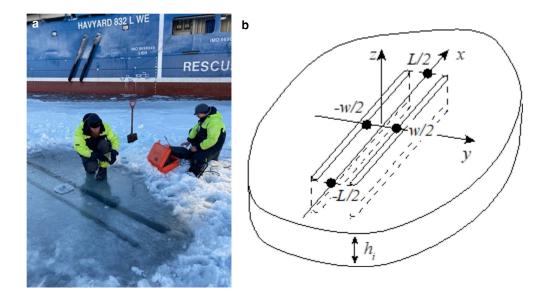


Figure 2. (a) Fixed-ends beam in landfast ice of Tempelfjorden. (b) Schematic of the test with vibrating floating fixed-ends beam.

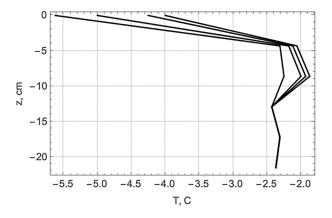


Figure 3. Temperature profiles recorded for 5 min for a total duration of 20 min through the sea ice covered by thin snow layer.

Accelerations caused by five hits of the beam are well visible in Figure 5a. Figure 5b shows the recorded accelerations up to 0.5 s after the hits were initiated (lines 2–5 are shifted upward for visual purposes), indicating oscillations are the same for each event. Figure 6a shows the spectra of the accelerations recorded during events 1–5, and Figure 6b shows the mean spectrum. One can see that all spectra peaks are located at ~17 Hz. Numerical simulations indicated that eigenfrequency of the fixed-ends beam is 17 Hz when the elastic modulus is of ~1.1 GPa (Supplementary material).

Figure 7a shows the beam accelerations recorded during 2 s before the first hit shown in Figure 5a. Vibrations of the beam are well visible and spectral analysis shows that the frequency of vibrations was 15.5 Hz in both events I and II (Fig. 4a) without hits. Figure S3b indicates the elastic modulus of 0.9 GPa when the eigenfrequency equals 15.5 Hz. The influence

of ice viscosity on the eigenfrequency is expected to be insignificant since the relaxation time of sea ice taken from landfast ice of Spitsbergen fjords was estimated of several tens of seconds and greater (Voermans and others, 2021; Marchenko and others, 2023), which is much larger the period of eigen oscillations of the beam. We may thus conclude that the elastic modulus measured in the test with floating vibrating beam was of about $E \approx 1$ GPa.

Data analysis

Source triangulation was used to determine where the vibrations originate from and at what speed the vibrations were propagating. The arrival times of vibration events at the location of the geophones may be determined by:

$$t_{1} = t_{0} + \sqrt{(x_{1} - x_{0})^{2} + (y_{1} - y_{0})^{2}}/c$$

$$t_{2} = t_{0} + \sqrt{(x_{2} - x_{0})^{2} + (y_{2} - y_{0})^{2}}/c$$

$$t_{3} = t_{0} + \sqrt{(x_{3} - x_{0})^{2} + (y_{3} - y_{0})^{2}}/c$$
(1)

where t refers to time and (x, y) the coordinates in a relative frame of reference and c is the propagation speed of the waves. Subscripts refer to the geophone (1–3) or the source (0), i.e. t_1 is the instant at which a vibration event arrives at the location of geophone 1 at (x_1, y_1) . Equation (1) contains four unknowns (namely, t_0, x_0, y_0 and c) and thus would normally require four geophones to identify where the vibrations are coming from. However, if information is known about the speed at which these vibrations propagate, one more equation is available and the source of the vibration event can be determined with three geophones. In the case of compressive and shear waves, the

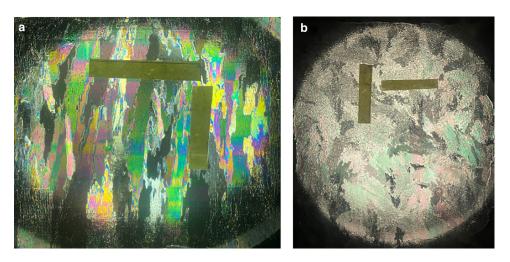
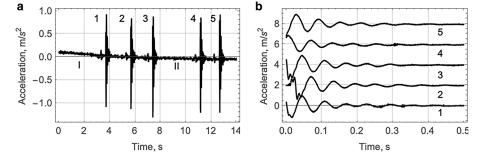


Figure 4. Photographs of (a) vertical and (b) horizontal thin sections of sea ice in polarized light. Thin sections were made from a specimen of sea ice from the Tempelfjorden, March 2022. Yellow strips scale 5 cm length.

Figure 5. (a) Record of vertical accelerations of the fixed-ends beam versus time during the five events (1–5) initiated by hits of the beam. (b) Zoomed-in records of the acceleration versus time during the five events.



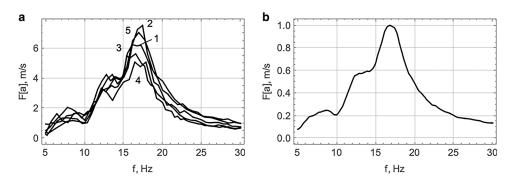


Figure 6. (a) Spectra of acceleration recorded during events 1-5. (b) The mean spectrum of the acceleration.

wave speed is given, respectively, by Stein and others (1998):

$$c_{\rm c} = \sqrt{\frac{E}{\rho_{\rm f}(1-\theta^2)}}$$

$$c_{\rm s} = \sqrt{\frac{E}{2\rho_{\rm c}(1+\theta)}}$$
(2)

where θ is the Poisson ratio, here taken as 0.3 (e.g. Timco and Weeks, 2010). For flexural waves in sea ice we assume the ice to be a thin elastic plate such that the dispersion relation of flexural waves in ice can be modeled as (Fox and Squire, 1991; Collins and others, 2017):

$$\frac{\omega^2}{Lk^4/\rho_{\rm w} - M\omega^2 + g} = k \tanh{(kd)}$$
(3)

with $L = E^*H^3/(12[1 - \theta^2])$, $M = H\rho_i/\rho_w$, where $\omega = 2\pi/T$ is the angular frequency with wave period *T*, the wave number *k* and water depth *d*. From Eqn (3) the propagation speed of wave energy of flexural waves (the group velocity c_g) can be determined as $c_g = \partial \omega / \partial k$. We note that Eqn (3) introduces two additional unknowns, the ice thickness *H* and effective elastic modulus E^* . However, as flexural waves are dispersive, observations of t_1 , t_2 and t_3 across a wide range of wave frequencies may provide enough information to determine x_0 , y_0 , *H* and E^* (e.g. Moreau and others, 2020b).

We use here two different approaches in estimating the elastic modulus of the ice and the source of vibration events. We focus for this on flexural waves. The first approach considers the difference in arrival times of vibrations with frequency *f* between pairs of geophones to estimate the group velocity as $c_{g,ij}(f) = \left(\sqrt{(x_i - x_0)^2 + (y_i - y_0)^2} - \sqrt{(x_j - x_0)^2 + (y_j - y_0)^2}\right)/(t_i - t_i)$, where *i* and *j* refer to the geophone numbers. For this,

 $(t_i - t_j)$, where *i* and *j* refer to the geophone numbers. For this, arbitrary (x_0, y_0) are taken to estimate $c_g(f)$ for each pair, where solutions for $c_g(f)$ and (x_0, y_0) are found when $c_{g,12} = c_{g,13} = c_{g,23}$. For different *f*, this provides observations of c_g across

a range of f to which the dispersion relationship Eqn (3) can be fitted. For the second approach, Eqns (1) and (3) are solved iteratively to obtain the lowest RMSE in t_1 , t_2 and t_3 with variable (x_0 , y_0 , t_0), H and E^* . We note that alternative approaches exist to the minimum RMSE approach, such as Bayesian inference (Moreau and others, 2023). The first approach may be seen as local as the phase speed of the vibrations are estimated locally at the site of the geophones, while the second approach may be viewed as non-local as the sea-ice properties between the vibration source and the geophones will influence the results.

Results

In this study, we focus on three major events that were recorded on the 18th, 21st and 22nd of February by all three geophones. We refer to these events as I-III, respectively. In Figures 8a, b the time series of the y- and z-components of geophone 3 during event III are shown. We note that events I and II have similar characteristics as event III, except that the magnitude of the vibrations recorded during event III were the largest. At around t = 170 s, high-frequency vibrations are observed, followed by low-frequency waves over the next few hundred seconds. The high-frequency vibrations are strongest in the horizontal direction and relatively weak in the vertical component, suggesting this may be a compressive wave. The low-frequency waves induces surface velocities similar in magnitude in both horizontal and vertical directions. While magnitude of the voltage amplitudes from t = 400 to 550 s as observed in Figure 8b is increasing, we reiterate that this is not directly translatable to an increased amplitude of the surface elevation of the ice as the geophones response to low frequencies is not linear. In Figure 8c the corresponding time series of sound pressure recorded by the hydrophone is shown. We note that we have shifted the time series of the hydrophone recordings by 65 s to match the records of the geophone loggers. This shift is caused by clock drift as the hydrophone logger, unlike the geophone loggers, is not synchronized by GPS. Based on the audio records, we suspect the event to originate

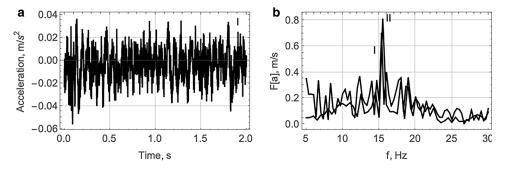


Figure 7. (a) Accelerations of the beam center versus time during event I. (b) Spectra of the beam accelerations recorded during events I and II.

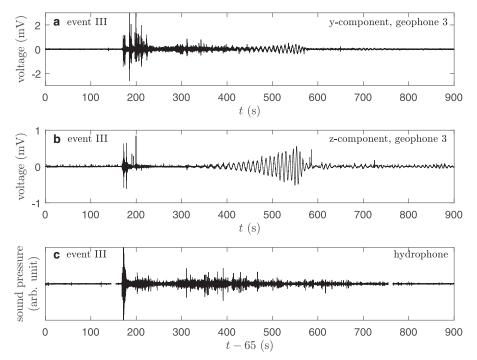


Figure 8. Time series of (a) horizontal and (b) vertical vibrations recorded by geophone 3 during event III. A high-frequency event around t = 200 s is closely followed by low-frequency waves between t = 300 and 600 s. Note that the vertical axes are scaled differently. Hydrophone recording during is shown in (c) shifted by 65 s, a shift originating from clock drift of the hydrophone logger, to match the time of the initial vibrations recorded by the geophone loggers.

from the glacier and caused by calving (a snapshot of the audio record during this initial event can be found at http://doi.org/ 10.5281/zenodo.7750699).

In Figure 9 the continuous wavelet transform is shown of the time series presented in Figure 8a. The initial vibrations around t = 200 s are within a frequency range of 0.4–18 Hz and do not appear to be dispersive. To obtain information on the times at which these high-frequency vibrations arrived at the geophones, we cross-correlate between the horizontal components of geophone pairs to estimate the transit time of the initial high-frequency vibrations between these pairs, i.e. this will provide estimates of $t_1 - t_2$, $t_1 - t_3$ and $t_2 - t_3$. Following the first approach (see 'Data analysis' section), we estimate the propagation speed of these initial vibrations to be 2178, 2184 and 2321 m s⁻¹ for events I–III, respectively, and are coming from the direction of the glacier. We suspect that these vibrations are compressive waves and thus do not satisfy the frequency dispersion relation of Eqn (3).

As the low-frequency waves that follow the initial high-frequency vibrations appear to be dispersive (see Fig. 9), and

the waves are unlikely to have been generated in the open water, we can obtain the f-t relationship from the wavelet spectrum. For this, we use the wavelet synchrosqueezed transform using Matlab's wsst-function and bump wavelet to identify the times of maximum energy at each frequency (Fig. 10). We note that minima in $c_{\rm g}$ (or maxima in t) can be observed around ~0.14 Hz. From the transit times between each geophone pair and for each wave frequency we can then estimate c_g as a function of f. In Figure 11a estimates of c_g are compared against the wave dispersion model in sea ice (Eqn (3)) for various values of the ice thickness *H* and effective elastic modulus E^* . For waves with $f \leq 0.1$ Hz the propagation speed of waves is largely unaffected by the ice. Notable deviations start to occur for $f \ge 0.11$ where thicker ice and a larger effective elastic modulus lead to increases in $c_{\rm g}$. Knowing that the ice thickness near the geophones was measured at ~0.5 m, our initial estimate of E^* is 1.4 GPa. This is, however, strongly based on the observations during event I and the frequency range 0.16-0.2 Hz. From the transit times between geophone pairs, i.e. t_1

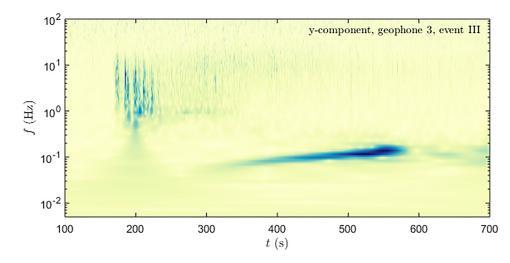


Figure 9. Continuous wavelet transform of the time series shown in Figure 8a. Color is indicative of the energy, with blue indicating high energy and yellow low energy.

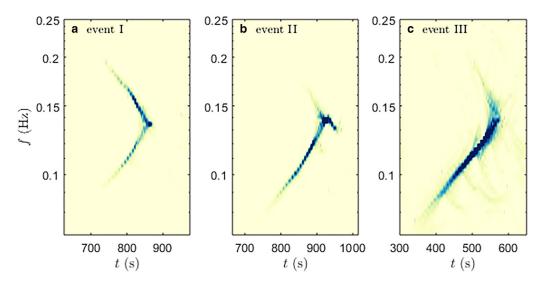
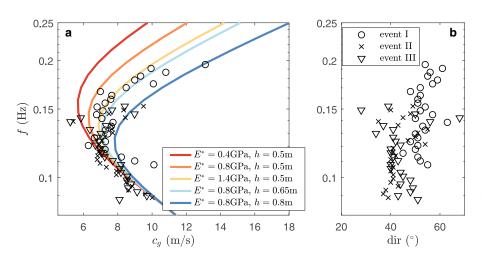


Figure 10. Wavelet synchrosqueezed transform of the y-component of geophone 3 during events (a) I, (b) II and (c) III, respectively. Color is indicative of the energy, with blue indicating high energy and yellow low energy.



 $-t_2$, $t_1 - t_3$ and $t_2 - t_3$, we can also identify the direction of the source of the waves relative to the geophones (Fig. 11b). Assuming that all waves are supposed to come from the same source for each event, and thus same direction for each event, it suggests that uncertainty in estimates of c_g is largest for the higher frequencies.

In Figure 12 the dispersion relationship is fitted directly to the observed f-t curves following the second approach (see 'Data analysis' section) to obtain best estimates of H and E^* . The observations match the dispersion relationship of waves in ice well, although the minima in $c_g(f)$ (or maxima in t(f)) tend to be overpredicted (underpredicted). This may, however, also be an artifact of the wavelet synchrosqueezed transform.

As impacts of E^* and H on c_g are similar for frequencies smaller than about $f \leq 1$ Hz, multiple combinations of E^* and H can approximate the observations well (Fig. 13). Noting that the ice thickness around the geophones was measured at $H \approx 0.5$ m thick, and ice thickness near the glacier may be estimated at about $H \approx 0.75$ m based on extrapolation of the ice thickness measurements (a value similar to those measured near the glacier in 2011, e.g. Marchenko and others, 2011), the average ice thickness through which the vibrations traveled to reach the geophones is ~0.63 m. This would result in best estimates of the elastic modulus as 0.67, 0.64 and 0.42 GPa for events I–III, respectively. This is lower than the measured value of the purely elastic modulus $E \approx 1$ GPa at the ice edge from the beam experiments (see 'Elastic modulus' section).

Figure 11. (a) Estimates of group velocity as determined by the transit time between the three geophones for the three wave events. In color are given various estimates of the group velocity based on different effective elastic modulus E^* and sea-ice thickness H. (b) Estimates of the direction of the wave source relative to the geophones, where north is taken as 0°.

The source of the vibrations can be approximated by finding the lowest RMSE fit of the dispersion relation against the f-tcurve. Specifically, we find a global minimum for (x_0, y_0) for all three dispersive wave events. Contours of the RMSE for event III are shown in Figure 14 with a best estimate location of the vibration source located near the glacier wall, confirming that the events are originating from the glacier. In Figure 15 the best-estimate source locations of all three events are shown, including the direction of the source of the high-frequency vibrations. We note that the direction of the high-frequency vibration is based on a single data point and is thus expected to be less accurate than the estimate based on the low-frequency waves. They are, nevertheless, consistently directed toward the glacier.

Discussion

In this study, we estimated the effective elastic modulus from wave observations. We find that the effective elastic modulus derived from fitting the observed wave arrival times to the modeled arrival times retrieves estimates of 0.4–0.7 GPa, whereas estimates based on observations of the group velocity leads to a value of ~1.4 GPa. We believe the former is more accurate given that it uses considerably more data to perform the fitting. Particularly, we see scatter in the direction estimates of the vibration sources relative to the instruments for the higher frequency range (i.e. Fig. 11b), a range fundamental in the fit against the dispersion relationship

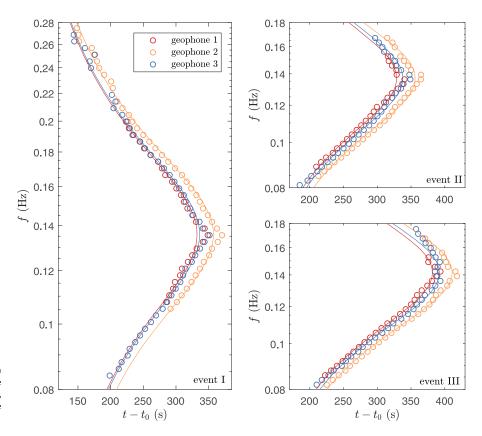


Figure 12. Best fits of the dispersion relationship in sea ice (solid line) against observed arrival times at the three geophones for the three events (markers). Note, multiple solutions exist for $H-E^*$ that can replicate the best fit, see Figure 13.

in ice. However, part of this difference could, possibly, be attributed to the variability of sea-ice conditions, in particular the sea-ice temperature. The sea-ice temperature near the ice edge was measured between -2.5 and -1.5° C (see Fig. 3), and expected to be much lower near the glacier between -15 and -10° C. Considering either of these estimates, our results suggest that the usage of a default value of $E^* = 5.5$ GPa in wave-ice interaction models may lead to significant errors and/or uncertainties in model simulations as those measured in this study are significantly lower. Further field experiments need to be performed, however, to provide more information on the variability of E^* in the field and to provide further recommendations on how to parameterize E^* .

While our observations were able to provide estimates of $H-E^*$ combinations, details on the ice thickness were required before E^* could be estimated explicitly. This is largely because the impacts

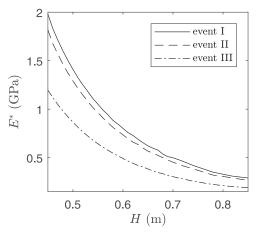


Figure 13. Best fit solutions to the wave arrival times as measured by the three geophones for the effective elastic modulus *E*^{*} and sea-ice thickness *H*.

of E^* and H on the shape of the dispersion relationship are indistinguishable for the frequency range of 0.08–0.28 Hz. To illustrate, in Figure 16 we compare $\Delta c_g = c_g - c_{g,ref}$ for different points on the $H-E^*$ curve for event III (see Fig. 13), with $E^* = 0.7$ GPa and H =0.54 m taken as the reference group velocity $c_{g,ref}$. Up to $f \approx 1 \text{ Hz}$ the different combinations of $H-E^*$ have very limited impact on the shape of $c_{g}(f)$, meaning that the absolute differences in c_{g} for different $H-E^*$ combinations are well within the measurement uncertainty of c_g . However, if observations are available for f > 1Hz, the range of $H-E^*$ solutions may be reduced significantly as differences in the group velocities between different solutions may exceed 1 m s⁻¹, while for observations of f > 10 Hz we expect that explicit estimates of E^* and H become feasible. Although the dispersive waves presented in this study (i.e. Fig. 8) do not contain significant or identifiable energy at f > 0.3 Hz, we note that measurements of dispersive waves at a higher frequency range are frequently encountered in our dataset. For instance, in Figure 17 an example of vibrations caused by a sequence of suspected (thermal) cracks is shown with identifiable phase-time information extending beyond 10 Hz. Usage of such higher frequency vibration events to estimate sea-ice properties was done successfully by others (e.g. Moreau and others, 2020b; Serripierri and others, 2022). Unfortunately, no further information of $H-E^*$ could be obtained from these data here as these cracking signals were only identifiable in the z-components of the geophones while only two geophones had this component working. Nevertheless, from the continuous wavelet transform we can see that the events arrived first at geophone 2 and we can infer from the data that, taking $E^* = 0.6$ GPa and H = 0.52 m, the source of these cracking events was ~110 m from geophone 2 and 260 m from geophone 3 (see dashed lines in Fig. 17).

Observations of the elastic modulus from wave observations thus far referred to the effective elastic modulus. However, from the propagation speed of compressive and shear waves in the ice, one may estimate the purely elastic modulus as well (i.e. Eqn (2)). From the direction of the x-y velocity vectors of

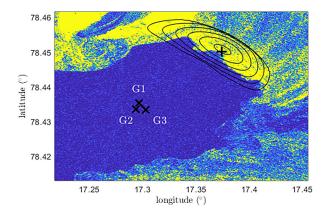


Figure 14. Estimates of the source of the dispersive waves during event III (plus sign) and associated contours of the RMSE of the best fits. Location of the geophones are identified by cross-markers. Sentinel-1 data image taken on 24-02-2022 is given in color.

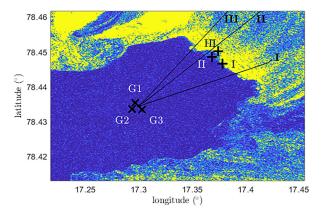


Figure 15. Estimates of the source of the dispersive waves during events I-III (plus markers) and direction of the high-frequency events (solid lines). Location of the geophones are identified by cross-markers. Sentinel-1 data image taken on 24-02-2022 is given in color.

the geophone signals we may approximate the direction of the initial high-frequency vibration events (Fig. 18). We note that the directions as observed by geophones 2 and 3 are well aligned with the direction from the geophones to the glacier for all three events which supports the hypothesis that the recorded high-frequency vibrations may be compressive waves. However, the direction of the vectors for geophone 1 during these events is consistently shifted by $50-60^{\circ}$ for unknown reasons, but we suspect that this is because an error in its alignment during deployment. If we were to assume that these are indeed compressive waves, from Eqn (2) the purely elastic modulus E is then estimated at 3.98, 4.00 and 4.52 GPa for events I-III, respectively. Evaluation of an additional 59 minor high-frequency events in the records shows consistent propagation speeds, with a mean of 2009 m s^{-1} and standard deviation of 180 m s⁻¹. This is much larger than the in situ estimates of 1 GPa from the beam experiments and we can only speculate on the reason of this difference. Our best guess is that the location and times at which these measurements were taken are too far apart for consistent interpretation. We note that the purely elastic modulus is always larger than the effective elastic modulus, except for very high loading rates where E^* will approach the value of *E*. We find here that *E* is \sim 2 and 5–6 times *E*^{*} for the in situ beam experiments and suspected compressive waves, respectively, and under the conditions experienced during the field experiment.

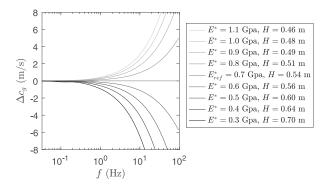


Figure 16. Variability of the group velocity $\Delta c_{\rm g} = c_{\rm g} - c_{\rm g}$, ref for combination solutions of $H-E^*$ with wave frequency. Here, $E^* = 0.7$ GPa and H = 0.54 m are taken for the reference velocity $c_{\rm g}$, ref. Impact of E^* and H to the shape of the dispersion relationship becomes significant for frequencies above 1 Hz.

For comparison, Karulina and others (2019) observed a difference by a factor of 4–5 between measurements of the elastic modulus obtained through cantilever experiments and direct acoustic observations.

Based on the geophone and hydrophone records, we suspect events I–III to originate from calving events at the glacier wall. The number of reported ice failure events in Spitsbergen glaciers is estimated to be in the range of 50–100 in February based on observations in 2010–12 (Fedorov and others, 2016), with most events not related to glacier wall calving and occur in the accumulation zone of glaciers. This seems to be consistent with our observations where only three significant events were recorded over a period of \sim 2 weeks. From this, we may also conclude that ice failure events at a distance from glacier front do not bring energy to the sea ice near the wall.

Although the observations of the low-frequency wave events fit well to the dispersion relationship of flexural waves in sea ice, there are limitations to the methodology used here. Most importantly, we assume here that the wave dispersion model of Fox and Squire (1991), i.e. Eqn (3), is valid. Second, we assume that the elastic modulus is constant over the ice thickness whilst this is, in general, not the case (e.g. Feltham and others, 2006). Third, our observations are most likely tsunami events caused by glacier calving, in analogy to landslide-induced tsunamis. The generation of such long waves at such proximity of the instruments are restricted to very limited sites across the polar regions. When waves are generated in open water and cross various types of sea ice, the cumulative impact of the inhomogeneous ice on the group velocity of low-frequency waves makes it problematic to estimate the effective elastic modulus based on the arrival times of waves (i.e. second approach, see 'Data analysis' section). In such a case, E^* can only be measured by estimating $c_{\rm g}$ from the transit times between the instruments (i.e. first approach, see 'Data analysis' section) or using accelerometers as done by, for example Voermans and others (2021) and Sutherland and Rabault (2016). Promising approaches that are applicable to sea ice in the MIZ are the derivation of the elastic modulus from dispersive high-frequency vibrations (e.g. Fig. 16) as demonstrated by Moreau and others (2020a, 2020b), Serripierri and others (2022) and Moreau and others (2023). On-board processing and remote data transmission will provide opportunities to increase the currently limited dataset of sea-ice property observations and accelerate the development of parameterizations based on system variables for operational wave forecasting models.

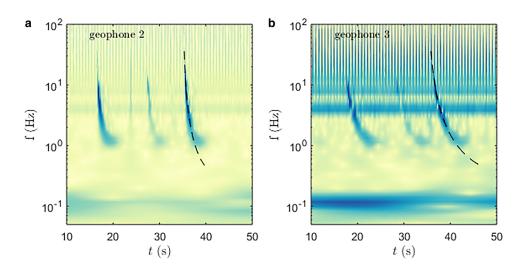


Figure 17. Example wavelet spectrum of the z-component of the geophone loggers during suspected cracking events. Black dashed line indicates best fit. Color is indicative of the energy, with blue indicating high energy and yellow low energy.

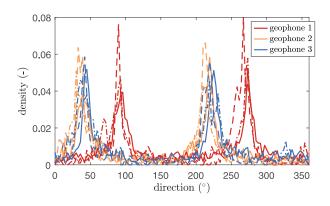


Figure 18. Probability density of the vector direction of initial high-frequency vibrations during event I (solid line), event II (dashed line) and event 3 (dash-dot line). North and east correspond to 0° and 90° , respectively.

Conclusions

We used observations of low-frequency dispersive waves to estimate the elastic modulus of landfast sea ice. By determining the arrival time of wave events at the geophones and their phase speed, we obtain estimates of the effective elastic modulus of 0.4–0.7 GPa. Estimates of the effective elastic modulus are lower than the purely elastic modulus measured in situ by beam experiments of 1 GPa. Our observation-based estimates of the elastic modulus are significantly lower than the default value of 5.5 GPa currently in use in contemporary wave models. While our observations are by no means representative for all sea ice, our results imply that considerable further efforts are required to increase the database of sea-ice property observations, including observations in the MIZ.

Supplementary material. The supplementary material for this article can be found at https://doi.org/10.1017/jog.2023.63

Acknowledgements. Alexander V. Babanin acknowledges support from the US Office of Naval Research grant N62909-20-1-2080. Joey J. Voermans and Alexander V. Babanin were supported by the Australian Antarctic Program under project 4593. Joey J. Voermans, Jean Rabault, Aleksey Marchenko, Takuji Waseda and Alexander V. Babanin acknowledge the support of the Research Council of Norway and Svalbard Science Forum under project 311266. The authors acknowledge that this work contains modified Copernicus Sentinel data 2022 processed by Sentinel Hub. The acoustic recording of the hydrophone during event III can be found at http://doi.org/10.5281/zenodo.7750699. Firmware and hardware design is made open-source

and can be found at http://github.com/jvoermans/Geophone_Logger. All data are made available in an online repository, visit the github repository for further directions on accessing the data or http://doi.org/10.21343/5vhg-a209. The authors thank Ludovic Moreau and an anonymous reviewer whose insightful comments have helped improve this manuscript.

Author contributions. Conceptualization: J.J.V., J.R., A.M., T.N., T.W., A.V.B.; methodology: J.J.V., J.R., A.M.; analysis: J.J.V., J.R., A.M.; writing – original draft: J.J.V.; writing – review and editing: J.J.V., J.R., A.M., T.N., T.W., A.V.B.; supervision: A.M., A.V.B.

References

- Ardhuin F and 6 others (2015) Estimates of ocean wave heights and attenuation in sea ice using the SAR wave mode on Sentinel-1A. *Geophysical Research Letters* 42(7), 2317–2325.
- Boutin G and 5 others (2018) Floe size effect on wave-ice interactions: possible effects, implementation in wave model, and evaluation. *Journal of Geophysical Research: Oceans* **123**(7), 4779–4805.
- Boutin G and 6 others (2020) Towards a coupled model to investigate wavesea ice interactions in the Arctic marginal ice zone. *The Cryosphere* 14(2), 709–735.
- Collins CO, Rogers WE and Lund B (2017) An investigation into the dispersion of ocean surface waves in sea ice. *Ocean Dynamics* 67(2), 263–280.
- **Collins III CO, Rogers WE, Marchenko A and Babanin AV** (2015) In situ measurements of an energetic wave event in the Arctic marginal ice zone. *Geophysical Research Letters* **42**(6), 1863–1870.
- Dumont D, Kohout A and Bertino L (2011) A wave-based model for the marginal ice zone including a floe breaking parameterization. *Journal of Geophysical Research: Oceans* **116**(4), C04001.
- Fedorov AV and 5 others (2016) Seismological observations of glaciers dynamic on the Spitsbergen archipelago. Vestnik MGTU 19(1), 151–159.
- Feltham DL, Untersteiner N, Wettlaufer JS and Worster MG (2006) Sea ice is a mushy layer. *Geophysical Research Letters* **33**(14), L14501.
- Fox C and Squire VA (1991) Strain in shore fast ice due to incoming ocean waves and swell. *Journal of Geophysical Research: Oceans* 96(C3), 4531–4547.
- Herman A (2021) Spectral wave energy dissipation due to under-ice turbulence. Journal of Physical Oceanography 51(4), 1177–1186.
- Herman A, Cheng S and Shen HH (2019) Wave energy attenuation in fields of colliding ice floes-part 2: a laboratory case study. *The Cryosphere* 13(11), 2901–2914.
- Horvat C, Blanchard-Wrigglesworth E and Petty A (2020) Observing waves in sea ice with ICESat-2. *Geophysical Research Letters* 47(10), e2020GL087629.
- Karulina M and 5 others (2019) Full-scale flexural strength of sea ice and freshwater ice in Spitsbergen fjords and North-West Barents Sea. Applied Ocean Research 90, 101853.
- Kohout AL and Meylan MH (2008) An elastic plate model for wave attenuation and ice floe breaking in the marginal ice zone. *Journal of Geophysical Research: Oceans* 113(C9), C004434.

- Kohout AL, Meylan MH and Plew DR (2011) Wave attenuation in a marginal ice zone due to the bottom roughness of ice floes. *Annals of Glaciology* 52 (57), 118–122.
- Kousal J, Voermans J, Liu Q, Heil P and Babanin A (2022) A two-part model for wave-sea ice interaction: attenuation and break-up. *Journal of Geophysical Research: Oceans* 127(5), e2022JC018571.
- Landau L and Lifshitz E (1975) Elastic waves. In *Theory of elasticity*. Oxford Pergamon Press, Oxford, UK, 116.
- Li J and 5 others (2021) Effects of wave-induced sea ice break-up and mixing in a high-resolution coupled ice-ocean model. *Journal of Marine Science and Engineering* 9(4), 365.
- Løken TK, Marchenko A, Ellevold TJ, Rabault J and Jensen A (2022) Experiments on turbulence from colliding ice floes. *Physics of Fluids* **34** (6), 065133.
- Marchenko A and 8 others (2011) Field studies of sea water and ice properties in Svalbard fjords. In *Proceedings of the International Conference on Port and Ocean Engineering under Arctic Conditions*, POAC11-148. Port and Ocean Engineering under Arctic Conditions, Montréal, Canada.
- Marchenko A, Morozov E and Muzylev S (2013) Measurements of sea-ice flexural stiffness by pressure characteristics of flexural-gravity waves. *Annals of Glaciology* 54(64), 51–60.
- Marchenko A, and 9 others (2020) Elastic moduli of sea ice and lake ice calculated from in-situ and laboratory experiments. In 25th IAHR International Symposium on Ice. International Association for Hydro-Environment Engineering and Research, Trondheim, Norway.
- Marchenko A, Karulin E, Chistyakov P, Karulina M and Sakharov A (2023) Meso-scale stress relaxation test on floating sea ice. In *POAC-23*. Port and Ocean Engineering Under Arctic Conditions, Glasgow, UK.
- Montiel F, Squire V and Bennetts L (2016) Attenuation and directional spreading of ocean wave spectra in the marginal ice zone. *Journal of Fluid Mechanics* **790**, 492–522.
- Moreau L and 9 others (2020a) Sea ice thickness and elastic properties from the analysis of multimodal guided wave propagation measured with a passive seismic array. *Journal of Geophysical Research: Oceans* 125(4), e2019JC015709.
- Moreau L, Weiss J and Marsan D (2020b) Accurate estimations of sea-ice thickness and elastic properties from seismic noise recorded with a minimal number of geophones: from thin landfast ice to thick pack ice. *Journal of Geophysical Research: Oceans* 125(11), e2020JC016492.
- Moreau L, Seydoux L, Weiss J and Campillo M (2023) Analysis of microseismicity in sea ice with deep learning and Bayesian inference: application to high-resolution thickness monitoring. *The Cryosphere* **17**(3), 1327–1341.
- Nelli F, Bennetts LG, Skene DM and Toffoli A (2020) Water wave transmission and energy dissipation by a floating plate in the presence of overwash. *Journal of Fluid Mechanics* 889, A19. doi: 10.1017/jfm.2020.75
- Nose T and 9 others (2023) A comparison of an operational wave-ice model product and drifting wave buoy observation in the central arctic ocean: investigating the effect of sea-ice forcing in thin ice cover. *Polar Science* 42.
- Oliver J, Crary A and Cotell R (1954) Elastic waves in Arctic pack ice. Eos, Transactions American Geophysical Union 35(2), 282–292.
- Pațilea C, Heygster G, Huntemann M and Spreen G (2019) Combined SMAP-SMOS thin sea ice thickness retrieval. *The Cryosphere* 13(2), 675–691.
- Rabault J, Sutherland G, Jensen A, Christensen KH and Marchenko A (2019) Experiments on wave propagation in grease ice: combined wave

gauges and particle image velocimetry measurements. Journal of Fluid Mechanics 864, 876-898.

- Rabault J and 5 others (2020) An open source, versatile, affordable waves in ice instrument for scientific measurements in the polar regions. *Cold Regions Science and Technology* 170, 102955.
- Rabault J and 9 others (2022) OpenMetBuoy-v2021: an easy-to-build, affordable, customizable, open-source instrument for oceanographic measurements of drift and waves in sea ice and the open ocean. *Geosciences* 12(3), 110.
- Rabault J and 9 others (2023) A dataset of direct observations of sea ice drift and waves in ice. *Scientific Data* **10**(1), 251.
- **Rogers WE, Meylan MH and Kohout AL** (2021) Estimates of spectral wave attenuation in Antarctic sea ice, using model/data inversion. *Cold Regions Science and Technology* **182**, 103198.
- Serripierri A, Moreau L, Boue P, Weiss J and Roux P (2022) Recovering and monitoring the thickness, density, and elastic properties of sea ice from seismic noise recorded in Svalbard. *The Cryosphere* 16(6), 2527–2543.
- Shen HH (2019) Modelling ocean waves in ice-covered seas. Applied Ocean Research 83, 30–36.
- Soler-Llorens JL and 5 others (2016) Development and programming of geophonino: a low cost Arduino-based seismic recorder for vertical geophones. *Computers Geosciences* 94, 1–10.
- Squire VA (2020) Ocean wave interactions with sea ice: a reappraisal. Annual Review of Fluid Mechanics 52, 37–60.
- Stein PJ, Euerle SE and Parinella JC (1998) Inversion of pack ice elastic wave data to obtain ice physical properties. *Journal of Geophysical Research: Oceans* 103(C10), 21783–21793.
- Sutherland G and Rabault J (2016) Observations of wave dispersion and attenuation in landfast ice. *Journal of Geophysical Research: Oceans* 121(3), 1984–1997.
- Timco G and Weeks W (2010) A review of the engineering properties of sea ice. Cold Regions Science and Technology 60(2), 107–129.
- Voermans J, Babanin A, Thomson J, Smith M and Shen H (2019) Wave attenuation by sea ice turbulence. *Geophysical Research Letters* **46**(12), 6796–6803.
- Voermans JJ and 9 others (2020) Experimental evidence for a universal threshold characterizing wave-induced sea ice break-up. *The Cryosphere* 14(11), 4265–4278.
- Voermans JJ and 9 others (2021) Wave dispersion and dissipation in landfast ice: comparison of observations against models. *The Cryosphere* 15(12), 5557–5575.
- Wang R and Shen HH (2010) Gravity waves propagating into an ice-covered ocean: a viscoelastic model. *Journal of Geophysical Research: Oceans* 115 (C6), C005591.
- Williams TD, Bennetts LG, Squire VA, Dumont D and Bertino L (2013) Wave-ice interactions in the marginal ice zone. Part 1: theoretical foundations. Ocean Modelling 71, 81–91.
- Williams TD, Rampal P and Bouillon S (2017) Wave-ice interactions in the neXtSIM sea-ice model. *The Cryosphere* 11(5), 2117–2135.
- WW3DG (2019). User manual and system documentation of WAVEWATCH III TM version 6.07. Tech. Note 333, NOAA/NWS/NCEP/MMAB, 465.
- **Yang T and Giellis G** (1994) Experimental characterization of elastic waves in a floating ice sheet. *The Journal of the Acoustical Society of America* **96**(5), 2993–3009.